Fusion Engineering and Design 194 (2023) 113736

Contents lists available at ScienceDirect

Fusion Engineering and Design

journal homepage: www.elsevier.com/locate/fusengdes

Study of positive ion transport to the plasma electrode in giant RF negative ion sources☆,☆☆

Beatrice Segalini [a,b,*], Carlo Poggi [a], Michele Fadone [a], Gianluigi Serianni [a,c], Emanuele Sartori [a,b]

[a] Consorzio RFX (CNR, ENEA, INFN, UNIPD, Acciaierie Venete SpA), Corso Stati Uniti 4, Padova, 35127, Italy
[b] Università degli Studi di Padova, via VIII Febbraio 2, Padova, 35122, Italy
[c] ISTP-CNR, Institute for Plasma Science and Technology, Corso Stati Uniti 4, Padova, 35127, Italy

ARTICLE INFO

Keywords:
Neutral beam injection
Negative ion sources
Monte Carlo simulations
Negative ions
Energy distribution

ABSTRACT

Negative ion sources are fundamental components of neutral beam injectors (NBI), one of the main heating systems for fusion reactors. SPIDER is the full-scale prototype negative ion source for ITER NBIs. It is hosted in Padua as part of the Neutral Beam Test Facility (NBTF). It aims to extract up to 330 A m^{-2} of negative hydrogen ions from an inductively coupled plasma, generated inside 8 cylindrical drivers. The negative ion production is enhanced by caesium evaporation inside the source.

In caesium-seeded negative ion sources, negative ions are produced close to the extraction apertures, and they are mainly generated by surface conversion of neutral atoms and positive ions impinging on the ion source walls, particularly on the plasma grid. The conversion yields depend on the energy distribution of these precursors, and so does the energy of those particles which are reflected as negative ions. The positive ion flow in the extraction region may also impact on the extraction probability of negative ions, via momentum transfer. Besides, in giant multi-driver RF sources such as SPIDER, a gradient of plasma potential is present in the expansion region Sartori et al. (2021), affecting the positive ion transport towards the caesiated plasma electrode and their energy.

To approach this complex problem, a 3D test-particle Monte Carlo code for tracing plasma motion in SPIDER was developed. Positive ions species are generated in different positions within the plasma source volume and are tracked under the influence of electric and magnetic fields. Then, Monte Carlo collisions are used to simulate the interaction with predetermined backgrounds of plasma and neutrals, with profiles derived from experimental data. The particles are traced until they hit the ion source walls. Finally, the energy distribution of the different particle species impinging on the plasma grid (PG) are determined, and used to assess the generation and the energy distribution of the produced H^-.

1. Introduction

Future nuclear fusion reactors require external heating systems in order to reach and maintain the temperature needed to achieve a net energy gain. ITER, the largest international collaboration aiming at achieving a net energy gain from nuclear fusion [1], will rely on up to three neutral beam injectors, among other heating systems. Each of them will deliver 16.5 MW of 1 MeV deuterium atoms to the reactor plasma. These atoms will be produced from negative hydrogen ions, extracted and accelerated from a plasma source. As the requirements for ITER NBIs have never been achieved altogether in a single machine, the test facility PRIMA (Padova Research on ITER Megavolt Accelerator) has been built at Consorzio RFX in Padova. It hosts two experiments, MITICA (Megavolt ITER Injector & Concept Advancement [2]), the full scale prototype of the entire NBI, and SPIDER (Source for Production of Ion of Deuterium Extracted from RF plasma [3,4]) the prototype of the plasma source alone.

SPIDER is a giant RF negative ion source, designed to extract and accelerate 46/40 A of H^-/D^- ions up to 100 keV. It is composed of 8

☆ This work has been carried out within the framework of the ITER-RFX Neutral Beam Testing Facility (NBTF) Agreement and has received funding from the ITER Organization. The views and opinions expressed herein do not necessarily reflect those of the ITER Organization.

☆☆ This work has been carried out within the framework of the EUROfusion Consortium, funded by the European Union via the Euratom Research and Training Programme (Grant Agreement No 101052200 — EUROfusion). Views and opinions expressed are however those of the author(s) only and do not necessarily reflect those of the European Union or the European Commission. Neither the European Union nor the European Commission can be held responsible for them.

* Corresponding author at: Università degli Studi di Padova, via VIII Febbraio 2, Padova, 35122, Italy.
E-mail address: beatrice.segalini@igi.cnr.it (B. Segalini).

https://doi.org/10.1016/j.fusengdes.2023.113736
Received 31 October 2022; Received in revised form 24 February 2023; Accepted 7 April 2023
Available online 13 April 2023

cylindrical drivers, capable of igniting the plasma through the inductive coupling with 4 radio frequency (RF) generators, each delivering up to 200 kW. The plasma then expands in the so called expansion region, towards one of the source walls, where a set of 1280 apertures are present (plasma grid, PG). A transverse magnetic field of the order of a few mT is generated by an electrical current flowing in the plasma grid. This field reduces the electron temperature in the vicinity of the plasma grid, thus increasing the survival probability of the negative ions.

Plasma-facing surfaces of negative ion sources are covered by a layer of caesium. Thanks to the low work function of the alkaline metal, the extracted of H^- (D^-) are mostly produced via surface conversion of positive and neutral particles [5]. The energy of these H^- precursors influences beam properties, such as beam divergence and uniformity.

Thus, studying the precursors trajectories and determining their energy distribution is important and useful in order to improve the source performances. In this work, a three dimensional test particle Monte Carlo simulator has been developed with this aim, focusing especially on deriving energy spectra and producing a useful numerical tool to investigate physical phenomena and compare experimental data, following the example of previous work such as [6].

In Section 2, the physical model is described, explaining which electromagnetic fields are considered, the process of particle generation, how collisions are treated. In Section 3, simulation analyses are presented, focusing on the effect of magnetic filter field and PG biasing and on the H^- yield computation. In Section 4, conclusions are drawn also discussing possible improvements of the model.

2. Model description

In this section, a general description of the model adopted for describing SPIDER will be found. The code is a written in a C++ framework and takes into account many physical aspects of the source, and the paper will cover respectively:

- in Section 2.1, a description of the electrical and magnetic fields implemented;
- in 2.2: particle initialization, i.e. how the set of starting particles is generated;
- in Sections 2.3 and 2.4: a description of how elastic and inelastic collisions are treated;
- finally, in 2.5, the main numerical aspects are quickly reported.

2.1. Plasma profiles and electromagnetic fields in SPIDER

In this work, all the plasma and electromagnetic field profiles are inferred from experimental data, with some educated guesses derived from previous measurements on SPIDER or on similar sources [7–9]. In the following, the z direction corresponds to the beam direction, from the driver towards the expansion region. The x coordinate is horizontal and the y coordinate is vertical.

The magnetic field $\vec{B}$ can be chosen to be either constant along any space direction or to have an x-component function of the z coordinate, according to the formula:

$$B_x = \frac{\alpha}{2}(B_{PG} - B_{DVR})\tanh\left(\frac{z - z_{flex}}{m} + 1\right) + \alpha B_{DVR} \quad (1)$$

where $B_{PG} = 5$ mT is the value of B at the PG, $B_{DVR} = 2$ mT is the value of B at bottom of the driver, $z_{flex} = 0$ mm is the coordinate of the flex point and $m = 0.1$ is the slope of the curve, α is a factor used to model the shape of the curve.

This z–profile mimics the measured profile of SPIDER magnetic field [8]. Two different values of α ($\alpha = 0.5$, $\alpha = 1$) are used in the simulations presented in this paper, those $|B_{field}|$ curves are represented in the bottom half of Fig. 1: the energy spectra collected in these 2 configurations will be then compared to see how the magnetic field affects positive ions.

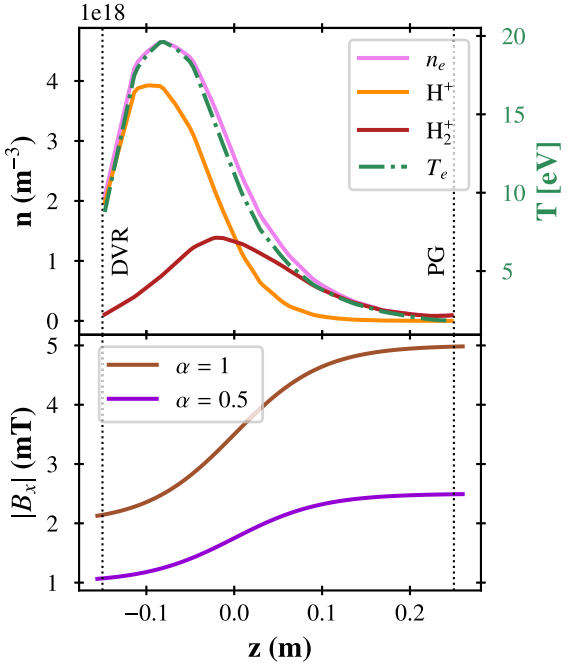

Fig. 1. Top: Background temperature and density profiles from the drivers to the PG. Bottom: module of the magnetic field x–component (horizontal) in the simulation domain.

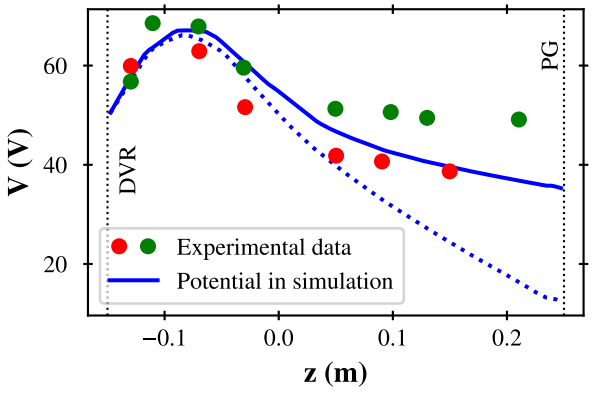

Fig. 2. Experimental potential profiles measured in SPIDER at $p = 0.3$ Pa, $P_{RF} = 50$ kW per driver, for bias voltage $ISBP = 14.3$ V (red) and $ISBP = 43$ V (green) (fig. 11 of [7]). The black dotted lines outlines the Plasma grid (PG) position and the driver back-plate (DVR), the potential at the PG is set to 35 V. The dashed line is a different configuration in which $V_{PG} = 12$ V.

Concerning the electric field, the potential profile is shaped to mimic experimental data of [7], collected with a set of movable Langmuir probes for 2 different bias plate voltages. In Fig. 2, two cases are depicted: a more realistic one (blue line, along z direction) and an extreme case, such as the dashed line in figure, which was also studied in order to show the impact of the potential shape on the energy distribution at the PG. The steepness of the curve in the expansion region impacts on the velocity of positive particles impinging on the grid, hence reflecting a change in the distribution and showing the strict relation between electrostatic potential and the energy distribution. This results will be addressed in Section 3 (Figs. 6, 7).

Tracking particles in the space potential does not need resolving the sheath thickness, therefore the potential imposed at the boundaries Σ is the potential at the plasma sheath edge $V_\Sigma = V_{sheath}$, with $V_{sheath} \approx V_{wall} + \frac{1}{2}\ln(m_+/m_e)\cdot T_e$ (i.e. not the potential of the metallic walls) at the driver walls, with T_e electron temperature, m_+ the positive ion effective

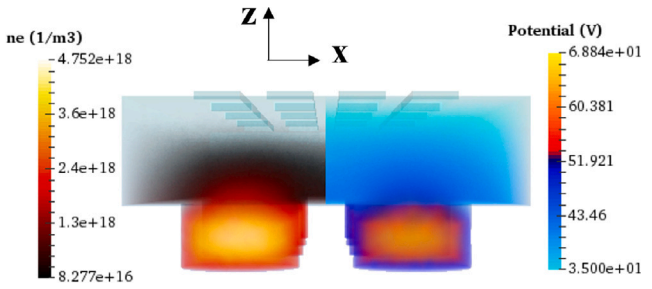

Fig. 3. Section of the simulation domain with potential and electron density 3D distribution.

mass and m_e the electron mass. This approximation is not necessarily applicable to the lateral walls and the PG, at which a fixed potential was applied, compatible with experimental measurements [7,10]. Then, the code computes the 3D space potential by solving Poisson equation. In order to obtain the fields in plasma, tailored 3D space charge distributions are chosen to mimic the experimental profiles $V(z)$, obtaining (for instance) the results in the right part of Fig. 3 ($x-z$ plane).

An approximate relation to yield the experimental profiles of electronic density along the driver's axis from the potential profile is obtained by fitting the experimental data with a polynomial function, $n_e = n_{e0}\{10^{17} + \sum_{i=1}^{4}(-1)^i a_i V^i\}$. The parameters are $a = 3.42\times10^{16}$, $a_2 = 1.75\times10^{16}$, $a_3 = 5.26\times10^{14}$, $a_4 = 4.73\times10^{12}$, while the maximum density n_{e0} can be defined (V is given in V, n_{e0} in 10^{17} m^{-3}). This relation is applied to derive the complete 3D distribution of the plasma parameters from the space potential. The electron temperature profile is also defined with a similar approach: the polynomial function is $T_e = \sum_{i=0}^{3} t_i V^i$ while the coefficients are $t_0 = 1.8$, $t_1 = 5.1\times10^{-2}$, $t_2 = 3.5\times10^{-2}$, $t_3 = -6.4\times10^{-4}$. An example of electron density profile is displayed in the top part of Fig. 1 and in the left part of Fig. 3. In the same figure, the H^+ and H_2^+ density distributions are also plotted: they are obtained from quasi-neutrality ($n_e = n_{H+} + n_{H2+}$) and assuming an effective mass $m_{eff} = 1 + \left(\tanh\left(z/l_0\right)+1\right)/2$ (with $l_0 = 10$ cm a characteristic length, which corresponds approximately to the dimension of the driver region) and to the electron density: $n_{H^+} = n_e(2 - m_{eff})$ and $n_{H_2^+} = n_e(m_{eff} - 1)$. This empirical formula is an educated guess based on [9], assuming a higher concentration of H^+, while H_2^+ are more dominant in the region close to the PG.

2.2. Spatial and energy distribution of starting particles

The velocities and energies of the initial set of particles, generated by dissociation of the background H_2 gas caused by electron impact, are defined according to an effective distribution that combines the various possible channels [11]. The electron temperature determines the various dissociation channels, so that the energy distribution function of the initial proton or atom varies within the simulation domain depending on the local electron temperature: for instance, at low electron temperature, dissociation via repulsive b^3 triplet state provides fragments with energy around 2.4 eV; at much higher electron energies, dissociative ionization via the repulsive state $2p\sigma_u$ of H_2^+ gives fragments with kinetic energy of about 4.3 eV. H_2^+ created by ionization have an initial energy of 0.1 eV. The generation of H, H^+ and H_2^+ is given from the reaction rates of neutral molecular hydrogen and electrons. The generation rates of the protons are significantly lower than the other particles. This is due to the fact that the threshold energy in protons production is significantly larger, meaning that the production of H or H_2^+ will prevail. Protons can however be produced by multi-step processes, as a product of H_2^+ interactions. For each test particle, its species is determined by comparing the generation probabilities: the rates $\langle\sigma v\rangle$ are multiplied by the electron and H_2 densities, by the volume of the mesh element in which the particle is born and divided by P, the number of test particles per mesh element. Hence, a weight associated to each of these particles is obtained: with this approach, the test particle weight depends on the background plasma and gas parameters, but can also be controlled by the mesh size. In Fig. 4, the aforementioned weights along the z direction are represented, highlighting the difference between the ones on driver axis and their value averaged on the source volume. The latter shows a discontinuity at the driver exit: this is due to the change in average plasma parameters when entering the expansion region.

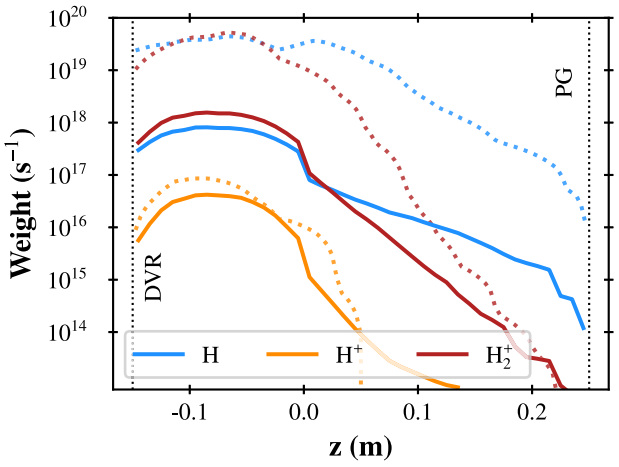

Fig. 4. Dotted lines: profile of starting test particle weights along a driver axis. Solid lines: starting test particle weights averaged on $x-y$ direction.

2.3. Elastic collisions

Elastic (Coulomb) collisions are treated following the small angle approach described in [12] (for neutrals) and in [13] (for Coulomb collisions between charged particles). Let the projectile be labeled with subscript 1 and the target with 2, and hence consider a system of two particles of mass m_1 and m_2 respectively, moving at speed v_1 and v_2 with respect to the laboratory inertial frame of reference. First of all, a change of frame of reference is performed, computing the particle velocities in the Center of Mass (CoM) system of reference, according to the formula:

$$\mathbf{v} = \frac{m_1\mathbf{v}_1 + m_2\mathbf{v}_2}{m_1 + m_2}. \tag{2}$$

Solving the equation of motion in this reference frame [14], it is possible to derive the exiting angles of the two particles after the collision:

$$\tan(\theta_1) = \frac{\sin\Theta}{m_1/m_2 + \cos\Theta} \tag{3}$$

$$\theta_2 = \frac{1}{2}(\pi - \Theta) \tag{4}$$

where Θ is the scattering angle in the CoM reference frame, which is selected randomly with a uniform distribution according to the null-collision method described in [12]:

$$\cos\Theta = 1 - 2R \tag{5}$$

with $R \in [0,1]$.

2.4. Inelastic collisions

To treat inelastic collision, let us consider the same two initial particles described at the beginning of Section 2.3. During the collision, a threshold energy $E_{th} > 0$ of the kinetic energy of the system is used to change the internal energy of one of the particles (e.g. in an ion-molecule collision, the molecule is excited to a higher vibrational state).

Table 1
Inelastic processes considered in the simulations.

Projectile	Target	Reaction results
H^+	H_2[v = 0]	$\longrightarrow H^+$, H[1s], H[1s]
H^+	H_2	$\longrightarrow H^+$, H_2^+, e
H^+	H_2	$\longrightarrow$ H, H_2^+
H^+	H[n = 1, 2, 3]	$\longrightarrow H^+$, H[n = 2, 3]
H^+	H[n = 1, 2, 3]	$\longrightarrow H^+$, H^+, e
H^+	H_2^+	$\longrightarrow H^+$, H, H^+
H	H_2	$\longrightarrow H^-$, H_2^+
H	H_2	$\longrightarrow$ H, H_2^+, e
H	H_2[v = 0, 1, 2]	$\longrightarrow$ H, H_2[v = 0, 1, 2]
H	H	$\longrightarrow H^-$, H^+
H	H	$\longrightarrow H^+$, H^+, e
H^+	H[n = 1, 2, 3]	$\longrightarrow H^+$, H^+, e
H^+	H[n = 1, 2, 3]	$\longrightarrow$ H[n = 1, 2, 3], H^+
e	H[1s]	$\longrightarrow$ e, H^+, e
e	H_2	$\longrightarrow$ e, H_2^+, e
e	H^-	$\longrightarrow$ H, 2e
H_2^+	H_2	$\longrightarrow H_2^+$, H_2^+, e
H_2^+	H_2	$\longrightarrow H_2$, H_2^+
H_2	H_2^+	$\longrightarrow H_2^+$, H_2
H^-	H_2	$\longrightarrow$ H, H_2, e
H^-	H_2	$\longrightarrow H^+$, H_2, e
H^-	H_2	$\longrightarrow H^-$, H_2^+, e
H^-	H_2	$\longrightarrow H^-$, H^+, H, e
H^-	H_2	$\longrightarrow H^-$, H^+, H^+, e
H^-	H	$\longrightarrow$ H, H^-
H^-	H	$\longrightarrow H_2$, e
H^-	H	$\longrightarrow H^+$, H, 2e
H^+	H^-	$\longrightarrow$ H, H
H^+	H^-	$\longrightarrow H_2^+$, e
H^+	H^-	$\longrightarrow$ H, H^+, e
H^+	H^-	$\longrightarrow H^+$, H^-

The energy and momentum conservation equations, in 3D, therefore are:

$$\frac{1}{2}m_1 v_1^2 + \frac{1}{2}m_2 v_2^2 - E_{th} = \frac{1}{2}m_1 v_1'^2 + \frac{1}{2}m_2 v_2'^2 \tag{6}$$

$$m_1 \boldsymbol{v_1} + m_2 \boldsymbol{v_2} = m_1 \boldsymbol{v_1'} + m_2 \boldsymbol{v_2'} \tag{7}$$

where $\boldsymbol{v_1}'$ and $\boldsymbol{v_2}'$ represent the velocities after the collision occurred.

The collision is defined as inelastic if it changes the state of one of the particles involved. Let the target particle (number 2) be the one changing its species, while the projectile (labeled with 1) remains unchanged. Moving to the target frame of reference by subtracting the velocity of particle 2 before the collision, we define $\widetilde{\boldsymbol{v_1}} = \boldsymbol{v_1} - \boldsymbol{v_2} = \boldsymbol{v_R}$, i.e. the relative velocity between the two particles and $\widetilde{\boldsymbol{v_2}} = 0$. The new conservation equations are:

$$\frac{1}{2}m_1 \widetilde{v_1}^2 - \widetilde{E_{th}} = \frac{1}{2}m_1 \widetilde{v_1'}^2 + \frac{1}{2}m_2 \widetilde{v_2'}^2 \tag{8}$$

$$m_1 \widetilde{v_1} = m_1 \widetilde{v_1'} + m_2 \widetilde{v_2'} \tag{9}$$

Notice that $\widetilde{E_{th}}$ and E_{th} are not necessarily equal [15].

Focusing on the energy equation, we can divide the collision in two steps:

1. Kinetic energy of particle 1 is transformed in internal energy of particle 2, and its velocity is reduced to [16]:

$$\widetilde{v_{1_{coll}}} = \widetilde{v_1}\sqrt{1 - \frac{\widetilde{E_{th}}}{\frac{1}{2}m_1 \widetilde{v_1}^2}} \tag{10}$$

2. Particle 1 then undergoes an elastic scattering collision with particle 2, according to equations:

$$\frac{1}{2}m_1 \widetilde{v}_{1_{coll}}^2 = \frac{1}{2}m_1 \widetilde{v_1'}^2 + \frac{1}{2}m_2 \widetilde{v_2'}^2 \tag{11}$$

$$m_1 \widetilde{\mathbf{v}}_1 = m_1 \widetilde{\mathbf{v}}_1' + m_2 \widetilde{\mathbf{v}}_2' \tag{12}$$

Transforming Eq. (10) to the laboratory frame of reference, it is possible to infer the relation between E_{th} and $\widetilde{E_{th}}$. The energy balance equation becomes:

$$\begin{aligned} E_{th} &= m_1 \boldsymbol{v_R} \cdot \boldsymbol{v_2}\left(1 - \sqrt{1 - \frac{\widetilde{E_{th}}}{\frac{1}{2}m_1 v_R^2}}\right) + \widetilde{E_{th}} \\ &\approx \widetilde{E_{th}}\left(\frac{\boldsymbol{v_R} \cdot \boldsymbol{v_2}}{v_R^2} + 1\right) \end{aligned} \tag{13}$$

where (13) holds for $\widetilde{E_{th}} \ll \frac{1}{2}m_1 v_R^2$. For the center of mass reference frame $\left(v_{CM} = \frac{m_1 v_1 + m_2 v_2}{m_1 + m_2}\right)$ the threshold energy is:

$$\begin{aligned} E_{th}^{CM} &= m_1 \boldsymbol{v_R} \cdot \left(\boldsymbol{v_2} - \boldsymbol{v_{CM}}\right)\left(1 - \sqrt{1 - \frac{\widetilde{E_{th}}}{\frac{1}{2}m_1 v_R^2}}\right) + \widetilde{E_{th}} \\ &= \widetilde{E_{th}}\left(\frac{\boldsymbol{v_R} \cdot \left(\boldsymbol{v_2} - \boldsymbol{v_{CM}}\right)}{v_R^2} + 1\right) = \widetilde{E_{th}}\frac{m_2}{m_1 + m_2} \end{aligned} \tag{14}$$

Inelastic collisions are picked between the ones reported in Table 1. They are treated by using the cross sections taken from many different Refs. [17–19] collected in a C++ library called `sammy`, originally developed for the use in particle-in-cell codes [20,21].

Probability of collisions with electrons, instead, are computed by using the rates and not the cross-sections. Rates are either the ones of [11] or are computed via another Monte Carlo simulation, independently, and stored in `sammy`.

2.5. Numerical implementation

The numerical framework is based on the ray tracing implementation of [23]. In this work, simulations are performed in a tetrahedral mesh composed of more than 15 000 elements, each of them with a determined volume. A user-defined number of particles is generated with a uniform spatial distribution inside each tetrahedron, following the approach reported in [24]. The dynamics is implemented via a Boris integrator [25]. Collisions are computed with the p−null method, adapted from [12].

One full simulation will produce a set of particle trajectories and a complete overview of the preset plasma parameters and boundary conditions, which can be visualized as in Fig. 5, which shows a typical simulation result: plasma background potential computed by solving 3D Poisson equations displays a higher potential in the driver which decreases along the z direction (as previously seen in Figs. 2, 3); some particle trajectories and their velocities are also shown.

3. Analysis and results

In this section, simulation results are presented and analyzed, focusing especially on energy profiles at the plasma grid.

3.1. Energy distributions at the plasma grid

Kinetic energy spectra are computed from the detected velocities of particles impinging the PG. Spectra can be divided by particle type, as reported in the two rows of Fig. 6. On the y axis, the flux energy variation, namely

$$\frac{d\Gamma}{dE} = \frac{dn}{dt} \cdot \frac{1}{A_{PG}} \cdot \frac{V_{elem}}{P} \frac{1}{dE} \tag{15}$$

is represented as a function of the particle kinetic energy, with V_{elem} volume of the mesh element, P the number of particles per mesh element, A_{PG} the plasma grid surface. In the top row, positive ion spectra are reported (H^+ in orange, H_2^+ in red), while in the bottom row fast neutral particles (H in blue, H_2 in magenta) are shown.

In the first 2 columns, a different line-style is used for representing two different magnetic field configurations: the dashed lines is the case with $\alpha = 0.5$ (namely $|B_{PG}| = 2.5\,\mathrm{mT}$), the solid lines is with $\alpha = 1$ ($|B_{PG}| = 5\,\mathrm{mT}$), corresponding to the profiles of Fig. 1. Note that the

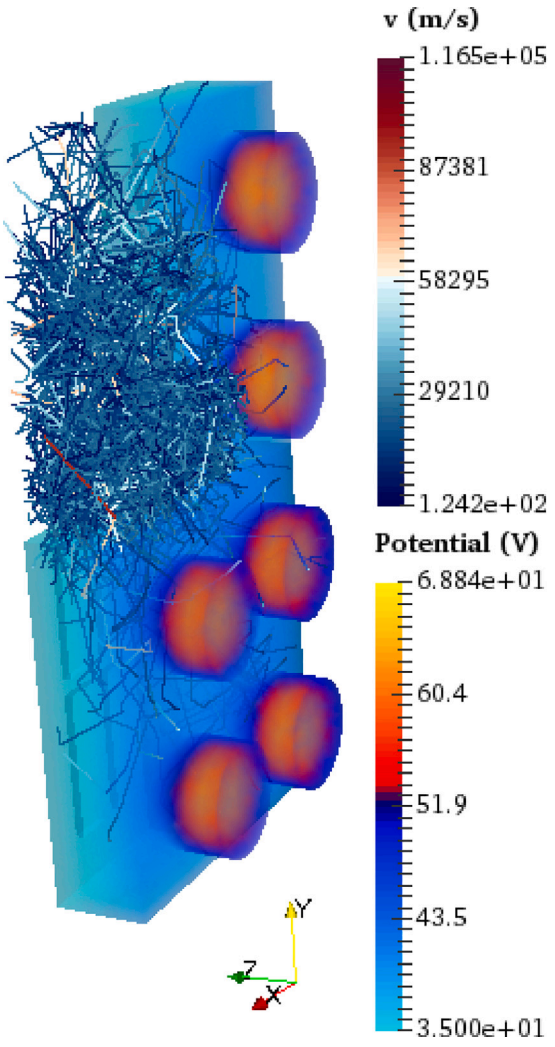

Fig. 5. Example of a simulation with particle trajectories, obtained with Paraview [22]. The 3D potential distribution computed by solving Poisson equations is reported, together with some particle trajectories (and their velocities).

thickest lines represent the simulations with the source parameters closest to the experimental conditions. In the column to the right, instead, the influence of the background gas density is analyzed, by comparing two different pressures. For simplicity, a fixed temperature for the H_2 background was taken, with $T_{H_2} = 800$ K, so that the density of the background gas can be obtained from the ideal gas law. In the figure, the dotted lines represent a simulation in which the pressure $p = 0.9$ Pa, while all the other data in Fig. 6 are computed with $p = 0.3$ Pa.

Firstly, let us focus on the positive ions, starting from the central column (graph **(b)**) of Fig. 6, corresponding to the solid line potential profile of Fig. 2. Broadly speaking, only the case of $\alpha = 1$ is reflecting the experimental conditions (hence the thicker line for highlighting it). The $\alpha = 0.5$ results are included to isolate the effect of magnetic filter field on the particle transport. In **(b)**, one can clearly notice the impact on ion energy distribution of the two different magnetic field configurations: with a less intense field (dashed lines), both H_2^+ and H^+ show a wide distribution with a peak centered at ≈13 eV for H^+ and at ≈20 eV for H_2^+. A factor 2 is present between the peaks intensity: heavier ions are the predominant charged species impacting on the PG, showing also a larger average energy. When we increase the magnetic field, and hence pass from the dashed to the solid line, both the distributions (but more evidently the H_2^+ one) display a change of their shape, in which we can now see two peaks. The lower energy one is for both species centered at ≈3 eV, while the predominant peak stays approximately in the aforementioned position (≈13 eV for H^+, ≈20 eV for H_2^+). This shows the presence of two different populations of ions, deriving from different source regions: this is evident if we consider Fig. 7, in which energy spectra are reported dividing the contributions from particles generated in different source regions. The code, in fact, stores the starting point of each test particle, and hence it is possible to recreate the spectra discriminating which particles are generated in the drivers (in blue), in the expansion region (orange) and in the final ten centimeters before PG (green). The latter are mostly irrelevant in the spectra: their contribution is barely visible and present only at low energies.

The interesting feature of these graphs is that particles originated in the expansion region are the main contributors of the low energy peak in the H_2^+ energy distribution, and are generally more present for $E_k < 10$ eV also in other particle spectra. In conclusion, we can observe that, for a lower magnetic filter field, the ion diffusion perpendicular to the field is higher, so that more charged particles impinge on the PG; however, one should consider that experimentally the electron density profile is also affected by the filter field, and this effect might be higher than in the simulated case for which the electron density profile is kept constant.

Let us now focus on a different potential profile. Fig. 6**(a)** shows the energy distribution for the case in which $V_{PG} = 12$ V (dotted line in Fig. 2), namely when the potential difference between the driver area and the PG is significantly steeper. In this case, the peak of the distribution is shifted at around 9 eV and the shape is more spread towards higher energies. This is due to the acceleration caused by the potential. The total ion flux is much larger (almost one order of magnitude) in this low-bias case with respect to the previous one. In addition, the effect of the magnetic field is different: unlike the large bias case, the stronger the field narrower the distributions, and the double peak structure does not appear, probably because in this configuration the potential shape dominates with respect to the filtering effect of the magnetic field. If we observe the origin of the particles composing these spectra (Fig. 8), one can notice a substantial difference with the previously studied case ($V_{PG} = 35$ V, Fig. 7). In fact, most of the particles reaching the PG are generated in the expansion region and not in the drivers: this means that, given the enhanced slope of the potential axial profile, particles are accelerated enough to arrive at the PG with sufficient energy and not be lost in collisions or on the source walls. Notably, the contribution of the driver-born particles is comparable with the one in Fig. 7. Furthermore, in the ion spectra (top row), the particles generated in the vicinity of the PG also have a more significant contribution.

The neutral particles (H, H_2) in both potential configurations are shown in graphs **(d)**, **(e)** of Fig. 6 and bottom row of Figs. 7, 8. One needs to notice that only fast H_2 derived from H_2^+ neutralization or charge exchange reactions are included in these graphs: the cold background component of the H_2 population is not considered. Neutrals are not influenced by a different magnetic field configuration, as expected, and both spectra show a peak at ≈3 eV. The intensity of the peak, however, changes with V_{PG}: the most drastic difference is for molecular hydrogen when changing the potential profile. The origin of neutral particles follow the changes previously displayed for the ions, with a bigger contribution of particles born in the expansion region for the $V_{PG} = 35$ V potential profile. Concerning these spectra, one should keep in mind that the graphs trace the location of the initial emission of the test particles, meaning that they do not take into account the location where a possible change of species due to inelastic collision occurred: this also explains why there is a significant population of neutral H_2 with $E_k > 10$ eV reaching the PG (bottom-right graph in Fig. 7).

Finally, another case studied concerns the comparison of energy distributions for two different pressures: by comparing graphs **(c)** and **(f)**, one can see that at higher pressures the flux of neutrals dominates

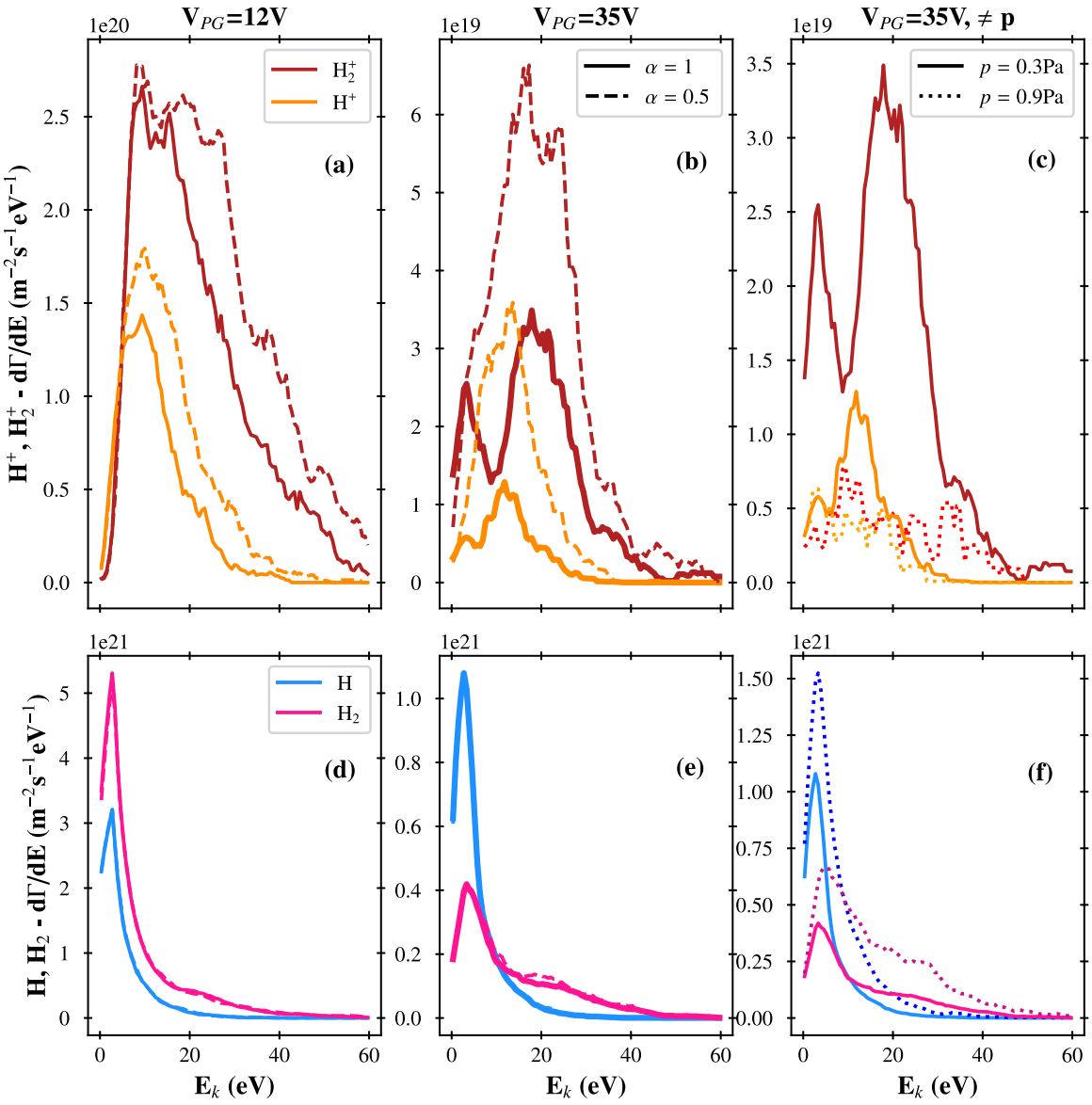

Fig. 6. Energy spectra of particle fluxes impinging the PG. **(a)**, **(b)**, **(c)** are positive ion spectra, while fast neutrals are presented in **(d)**, **(e)**, **(f)**. **(a)**, **(c)**: simulations with $V_{PG} = 12$ V (dotted line in Fig. 2) and with 2 different magnetic fields ($\alpha = 1$, solid line; $\alpha = 0.5$, dashed line). **(b)**, **(e)**: simulations with $V_{PG} = 35$ V (solid line in Fig. 2) and with 2 different magnetic fields ($\alpha = 1$, solid line; $\alpha = 0.5$, dashed line). **(c)**, **(f)**: simulations with $V_{PG} = 35$ V (solid line in Fig. 2) and with 2 different pressures ($p = 0.3$ Pa, solid line; $p = 0.9$ Pa, dotted line).

on the ions one by almost two order of magnitude, and while the shape of their energy distribution is mostly unchanged, the value of their maximum increases. Ion fluxes, on the other hand, are significantly lower: this because raising the pressure makes their neutralization more likely and hence less charged particles impact on the PG. This simulated case, however, does not take into account the true experimental conditions, in which the plasma parameters strongly varies when the pressure is tripled. Hence this comparison only needs to be considered as an unrealistic but informative example for the impact of the neutral background on the particle transport.

3.2. H^- conversion yields

Starting from the particle fluxes to the plasma grid, it is possible to estimate the negative ion yield. According to Seidl [26], H^- flux distribution generated from H, H^+, H_2^+ impinging on the PG is estimated via the yield equation:

$$Y = R_N \eta_0 \left(E_{in} - \frac{E_{th}}{R_E} \right) \tag{16}$$

with η_0, R_N experimental coefficients determined by the status of the caesiated surface. In this way, the spectra reported in Fig. 9 can be derived. The emission energy of negative ions is estimated as:

$$E_{k,H^-} = R_E E_{in} - E_{th} \tag{17}$$

with E_{th} the binding energy of the H^- ion, and R_E the reflection coefficient for the energy. It can be noticed that energetic negative ions are present in the distribution and that positive precursors mostly generate them. In the leftmost graph, a single narrow peak at 1–2 eV present, while in the H^+ and H_2^+ distributions the peak is wider and shifted more towards higher energies.

For H^+, the magnetic filter field has a clear impact: with the stronger field, the distribution maximum is at about 8 eV and the distribution is significantly more spread with respect to the low filter field configuration, where the width of the distribution is less than half and the peak is at ≈4 eV. For H_2^+ ions, instead, the different filter field does not move the peak position, but has an impact on the distribution width and the peak intensity, which doubles as α factor halves.

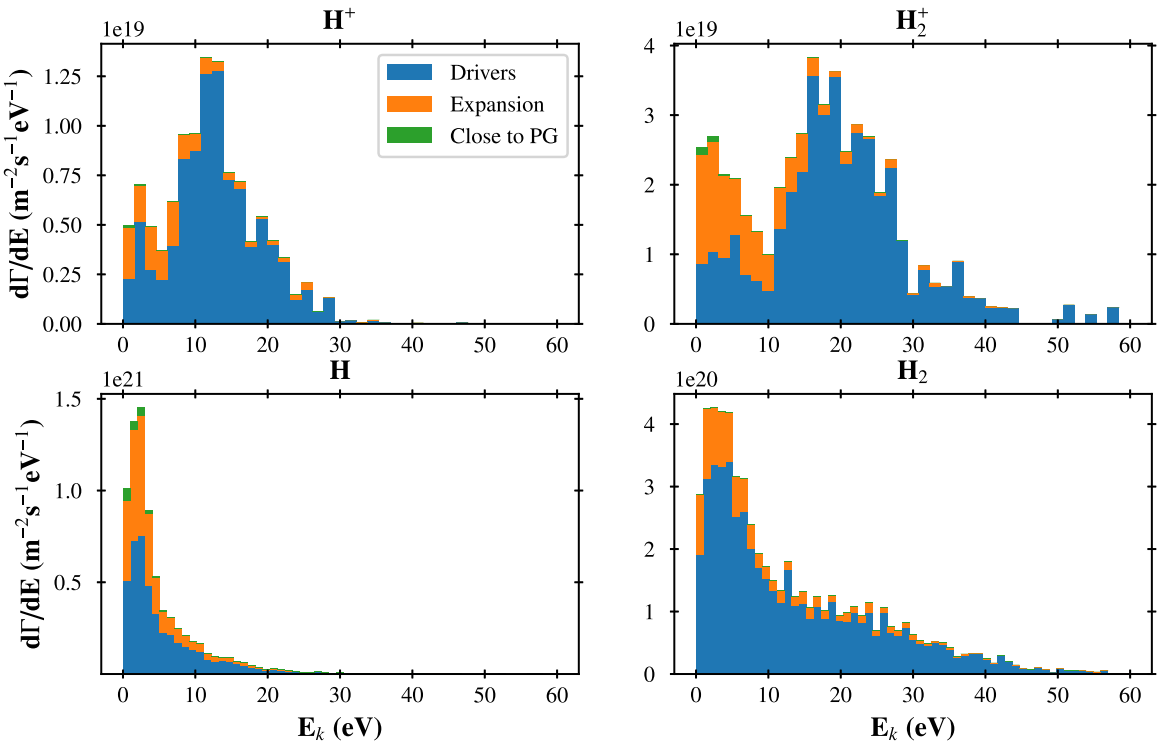

Fig. 7. Energy spectra of particle fluxes with different particle generation coordinate z, for the case of $V_{PG} = 35$ V and $\alpha = 1$. Different regions are represented by different colors and stacked one on top of the other.

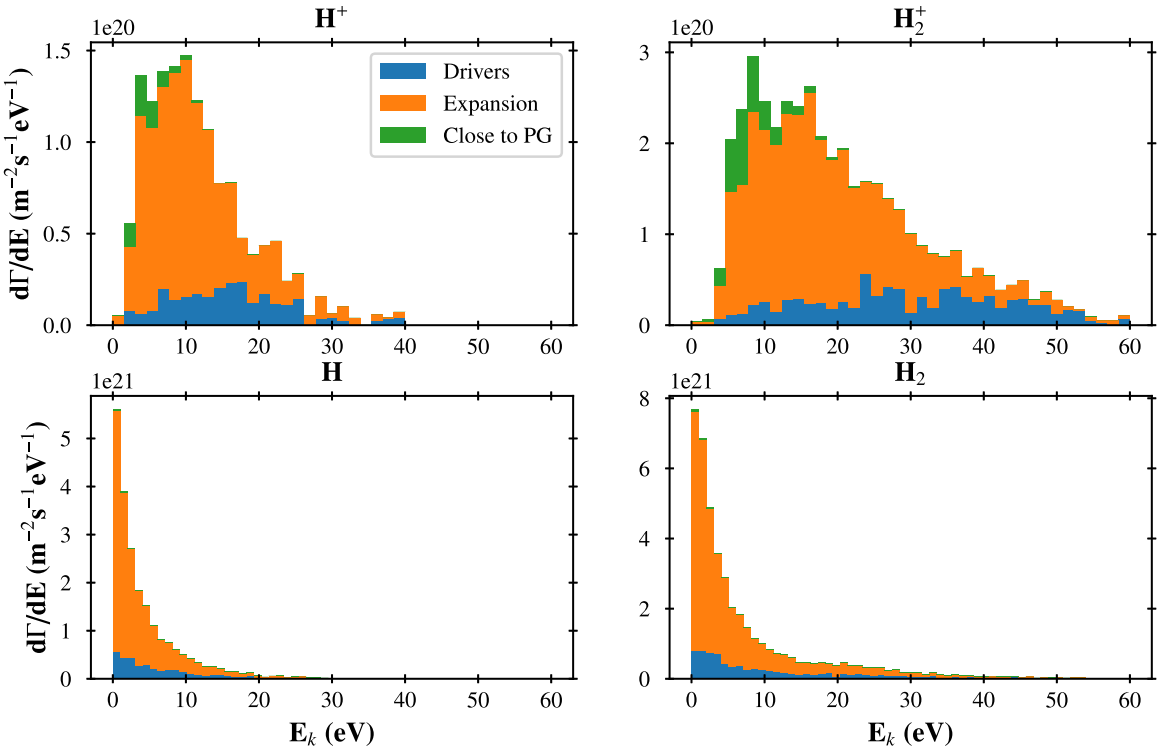

Fig. 8. Energy spectra of particle fluxes with different particle generation coordinate z, for the case of $V_{PG} = 12$ V and $\alpha = 1$. Different regions are represented by different colors and stacked one on top of the other.

3.3. Vertical profile of H flux onto PG

Within the approximations of the identical electron density distribution in each of the eight drivers, and of identical plasma profiles along the expansion region before the drivers, the three-dimensional simulation presented here allows to calculate the uniformity of the atom flux onto the plasma grid. Edge effects are identifiable at the top and bottom of the source, as shown in Fig. 10, even in this rather homogeneous case. The minima of the flux profiles are located behind the bias plate structure, which surrounds each of the 16 beamlet groups.

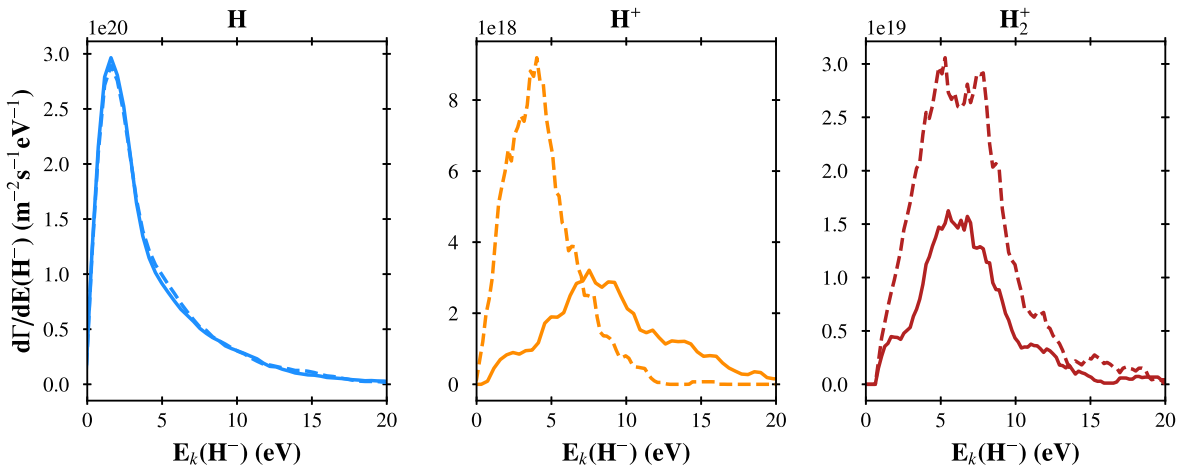

Fig. 9. H^- generated by H, H^+, H_2^+ energy distributions at the PG, computed via yield equation (16), for the case $V_{PG} = 35$ V. Solid lines: $\alpha = 1$; dashed lines: $\alpha = 0.5$.

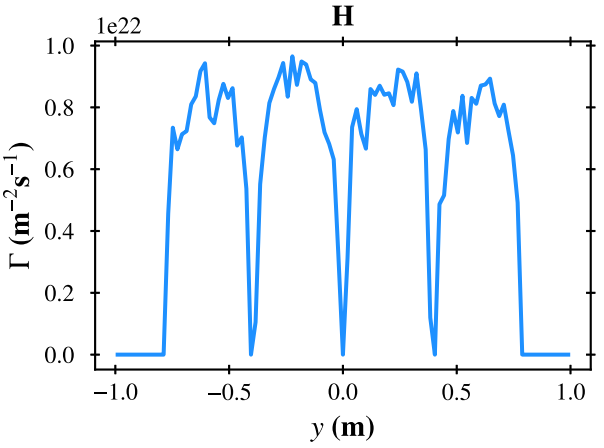

Fig. 10. Flux of neutral H impinging the PG.

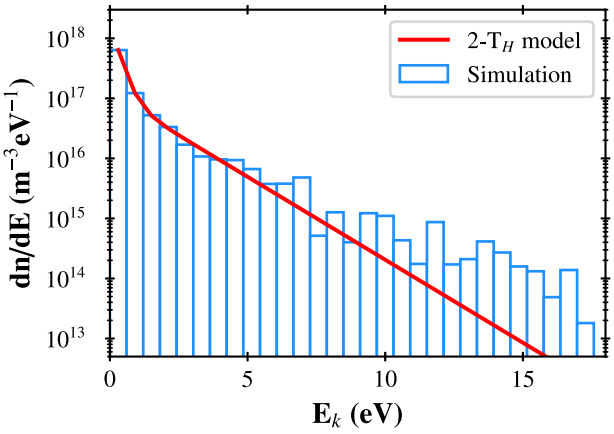

Fig. 11. Neutral H distribution at the plasma grid with fitting function for 2 different hydrogen populations ($T_H \approx 2.5$ eV, $T_H \approx 0.2$ eV).

If non-uniformities of the plasma were considered, such as those described in [27], a less regular picture of the atom flux could be obtained, with also left–right asymmetries.

3.4. H temperature before the PG

In this test-particle simulation, the parameters of the atomic population, which constitutes a target for the traced particles, are taken from experimental results [28], in which it is stated that neutral H population is divided into two parts characterized by two different temperatures. The energy distribution of test particles of species H within a control volume in front of the PG (blue bars) and the 2-temperature experimental model (red line) are presented in Fig. 11. It is possible to see that the distribution of the test particles resemble the properties of the background population, even though the initial energy of the test particles was determined by the dissociation events. This means that the properties assumed for the background are an equilibrium condition, and that the properties of the simulated test particles are determined by their relatively short mean free path at low energy (although this is not necessarily the case above 10 eV, as shown in the figure). On the other hand, the importance of the parameters assumed for the neutral H background is crucial, because they heavily impact particle transport. As an example, the existence of a H flow velocity has been neglected in this work, but it could have a role in particle fluxes impinging the PG.

4. Conclusion and future work

A test particle code was successfully developed to address transport of particles inside the plasma source of SPIDER. Energy distribution and charge state of particles impinging on PG were derived for many source parameter variations, one of which rather similar to an experimental condition ($V_{PG} = 35$ V, $\alpha = 1$).

The dependence on filter field and plasma parameters profiles was studied. Energy distribution widths obtained with this code are qualitatively in agreement with experimental measurements despite being different from similar codes previously developed [6]. The role of precursors in the negative ion production of the caesiated converter (i.e. plasma grid) was also addressed.

In future work, the positive ion energy distribution will be compared to experimental data collected via a RFEA, a diagnostic able to detect energy spectra [7]. Besides, data from other diagnostics, such as a Mach probe like the one described in [29], could also be used to improve the compatibility of simulations with the experimental data. Finally, the code shall be improved to track also hot atoms born on source walls, due to surface neutralization of H^+, H_2^+, H_3^+ or recombination of H.

Declaration of competing interest

The authors declare that they have no known competing financial interests or personal relationships that could have appeared to influence the work reported in this paper.

Data availability

Data will be made available on request.

References

[1] L. Grisham, P. Agostinetti, G. Barrera, P. Blatchford, D. Boilson, J. Chareyre, G. Chitarin, H. de Esch, A. De Lorenzi, P. Franzen, U. Fantz, M. Gagliardi, R. Hemsworth, M. Kashiwagi, D. King, A. Krylov, M. Kuriyama, N. Marconato, D. Marcuzzi, M. Roccella, L. Rios, A. Panasenkov, N. Pilan, M. Pavei, A. Rizzolo, E. Sartori, G. Serianni, P. Sonato, V. Pilard, M. Tanaka, H. Tobari, P. Veltri, P. Zaccaria, Recent improvements to the ITER neutral beam system design, Fusion Eng. Des. 87 (11) (2012) 1805–1815, http://dx.doi.org/10.1016/j.fusengdes.2012.08.001.

[2] P. Sonato, V. Antoni, M. Bigi, G. Chitarin, A. Luchetta, D. Marcuzzi, R. Pasqualotto, N. Pomaro, G. Serianni, V. Toigo, P. Zaccaria, I.I. Team, Status of PRIMA, the test facility for ITER neutral beam injectors, AIP Conf. Proc. 1515 (1) (2013) 549–558, http://dx.doi.org/10.1063/1.4792827, arXiv:https://aip.scitation.org/doi/pdf/10.1063/1.4792827. URL https://aip.scitation.org/doi/abs/10.1063/1.4792827.

[3] P. Sonato, P. Agostinetti, G. Anaclerio, V. Antoni, O. Barana, M. Bigi, M. Boldrin, M. Cavenago, S. Dal Bello, M.D. Palma, A. Daniele, M. D'Arienzo, A. De Lorenzi, A. Ferro, A. Fiorentin, E. Gaio, E. Gazza, L. Grando, F. Fantini, F. Fellin, A. Luchetta, G. Manduchi, F. Milani, D. Marcuzzi, L. Novello, R. Pasqualotto, M. Pavei, R. Pengo, S. Peruzzo, A. Pesce, N. Pilan, R. Piovan, N. Pomaro, M. Recchia, W. Rigato, A. Rizzolo, G. Serianni, M. Spolaore, P. Spolaore, S. Sandri, C. Taliercio, V. Toigo, M. Valisa, P. Veltri, P. Zaccaria, A. Zamengo, L. Zanotto, The ITER full size plasma source device design, Fusion Eng. Des. 84 (2) (2009) 269–274, http://dx.doi.org/10.1016/j.fusengdes.2008.11.095, Proceeding of the 25th Symposium on Fusion Technology. URL https://www.sciencedirect.com/science/article/pii/S0920379608004122.

[4] E. Sartori, M. Agostini, M. Barbisan, M. Bigi, M. Boldrin, M. Brombin, R. Casagrande, S.D. Bello, M. Dan, B. Duteil, M. Fadone, L. Grando, A. Maistrello, M. Pavei, A. Pimazzoni, C. Poggi, A. Rizzolo, A. Shepherd, M. Ugoletti, P. Veltri, B. Zaniol, R. Agnello, P. Agostinetti, V. Antoni, D. Aprile, V. Candeloro, C. Cavallini, R. Cavazzana, M. Cavenago, G. Chitarin, S. Cristofaro, M.D. Palma, R. Delogu, M.D. Muri, S. Denizeau, F. Fellin, A. Ferro, C. Gasparrini, P. Jain, A. Luchetta, G. Manduchi, N. Marconato, D. Marcuzzi, I. Mario, R. Milazzo, R. Pasqualotto, T. Patton, N. Pilan, M. Recchia, A. Rigoni-Garola, B. Segalini, M. Siragusa, M. Spolaore, C. Taliercio, V. Toigo, R. Zagorski, L. Zanotto, M. Zaupa, M. Zuin, G. Serianni, First operations with caesium of the negative ion source SPIDER, Nucl. Fusion 62 (8) (2022) 086022, http://dx.doi.org/10.1088/1741-4326/ac715e.

[5] M. Bacal, M. Wada, Negative hydrogen ion production mechanisms, Appl. Phys. Rev. 2 (2) (2015) 021305, http://dx.doi.org/10.1063/1.4921298.

[6] D. Wünderlich, L. Schiesko, P. McNeely, U. Fantz, P.F. and, On the proton flux toward the plasma grid in a RF-driven negative hydrogen ion source for ITER NBI, Plasma Phys. Control. Fusion 54 (12) (2012) 125002, http://dx.doi.org/10.1088/0741-3335/54/12/125002.

[7] E. Sartori, M. Brombin, B. Laterza, M. Zuin, R. Cavazzana, V. Cervaro, F. Degli Agostini, M. Fadone, D. Fasolo, L. Grando, P. Jain, M. Kisaki, A. Maistrello, G. Moro, A. Pimazzoni, C. Poggi, B. Segalini, A. Shepherd, M. Spolaore, C. Taliercio, M. Tollin, M. Ugoletti, P. Veltri, A. Zamengo, G. Serianni, Development of a set of movable electrostatic probes to characterize the plasma in the ITER neutral beam negative-ion source prototype, Fusion Eng. Des. 169 (2021) 112424, http://dx.doi.org/10.1016/j.fusengdes.2021.112424, URL https://www.sciencedirect.com/science/article/pii/S0920379621002003.

[8] N. Marconato, E. Sartori, G. Serianni, Numerical and experimental assessment of the new magnetic field configuration in SPIDER, IEEE Trans. Plasma Sci. (2022) 1–6, http://dx.doi.org/10.1109/TPS.2022.3167859.

[9] L. Schiesko, P. McNeely, P. Franzen, U. Fantz, the NNBI Team, Magnetic field dependence of the plasma properties in a negative hydrogen ion source for fusion, Plasma Phys. Control. Fusion 54 (10) (2012) 105002, http://dx.doi.org/10.1088/0741-3335/54/10/105002.

[10] C. Poggi, M. Spolaore, M. Brombin, R. Cavazzana, M. Fadone, R. Pasqualotto, A. Pimazzoni, N. Pomaro, E. Sartori, G. Serianni, C. Taliercio, Langmuir probes as a tool to investigate plasma uniformity in a large negative ion source, IEEE Trans. Plasma Sci. 50 (11) (2022) 3890–3896, http://dx.doi.org/10.1109/TPS.2022.3181805.

[11] E. Sartori, et al., Energy distribution of fragments in H2 dissociation by electron impact for the use in numerical models, in: NIBS'22 Conference, Journal of Instrumentation, 2022, submitted for publication.

[12] V. Vahedi, M. Surendra, A Monte Carlo collision model for the particle-in-cell method: applications to argon and oxygen discharges, Comput. Phys. Comm. 87 (1) (1995) 179–198, http://dx.doi.org/10.1016/0010-4655(94)00171-W, Particle Simulation Methods. URL https://www.sciencedirect.com/science/article/pii/001046559400171W.

[13] K. Nanbu, Theory of cumulative small-angle collisions in plasmas, Phys. Rev. E 55 (1997) 4642–4652, http://dx.doi.org/10.1103/PhysRevE.55.4642, URL https://link.aps.org/doi/10.1103/PhysRevE.55.4642.

[14] A.J.L. Michael A. Lieberman, Principles of Plasma Discharges and Materials Processing, second ed., 2005.

[15] R. Fitzpatrick, Two-body dynamics - scattering in the laboratory frame, 2011, URL https://farside.ph.utexas.edu/teaching/336k/Newton/node52.html.

[16] D. Tskhakaya, K. Matyash, R. Schneider, F. Taccogna, The particle-in-cell method, Contrib. Plasma Phys. 47 (8–9) (2007) 563–594, http://dx.doi.org/10.1002/ctpp.200710072, arXiv:https://onlinelibrary.wiley.com/doi/pdf/10.1002/ctpp.200710072. URL https://onlinelibrary.wiley.com/doi/abs/10.1002/ctpp.200710072.

[17] IAEA AMDIS ALADDIN Database, https://www-amdis.iaea.org/ALADDIN/.

[18] R. Janev, D. Reiter, U. Samm, Collision processes in low-temperature hydrogen plasmas, 2005, URL http://www.eirene.de/report_4105.pdf.

[19] P.S. Krstić, Vibrationally resolved collisions in cold hydrogen plasma, Nucl. Instrum. Methods Phys. Res. B 241 (1–4) (2005) 58–62, http://dx.doi.org/10.1016/j.nimb.2005.07.007.

[20] E. Sartori, T. Maceina, P. Veltri, M. Cavenago, G. Serianni, Simulation of space charge compensation in a multibeamlet negative ion beam, Rev. Sci. Instrum. 87 (2016) 02B917, http://dx.doi.org/10.1063/1.4933252.

[21] V. Candeloro, E. Sartori, G. Serianni, Electron scraping and electron temperature reduction by bias electrode at the extraction region of a large negative ion source, IEEE Trans. Plasma Sci. (2022) http://dx.doi.org/10.1109/TPS.2022.3171731.

[22] Paraview - Open-source, multi-platform data analysis and visualization application. URL https://www.paraview.org/.

[23] E. Sartori, A. Panasenkov, P. Veltri, G. Serianni, R. Pasqualotto, Study of a high power hydrogen beam diagnostic based on secondary electron emission, Rev. Sci. Instrum. 87 (2016) 11D438, http://dx.doi.org/10.1063/1.4960313.

[24] C. Rocchini, P. Cignoni, Generating random points in a tetrahedron, J. Graph. Tools 5 (4) (2000) 9–12, http://dx.doi.org/10.1080/10867651.2000.10487528, arXiv:https://doi.org/10.1080/10867651.2000.10487528.

[25] J.P. Boris, Relativistic plasma simulation-optimization of a hybrid code, in: Proceeding of Fourth Conference on Numerical Simulations of Plasmas, 1970.

[26] M. Seidl, H.L. Cui, J.D. Isenberg, H.J. Kwon, B.S. Lee, S.T. Melnychuk, Negative surface ionization of hydrogen atoms and molecules, J. Appl. Phys. 79 (6) (1996) 2896–2901, http://dx.doi.org/10.1063/1.361285, arXiv:https://doi.org/10.1063/1.361285.

[27] G. Serianni, E. Sartori, R. Agnello, P. Agostinetti, M. Agostini, M. Barbisan, M. Brombin, V. Candeloro, M. Dalla Palma, R. Delogu, M. De Muri, M. Fadone, I. Mario, T. Patton, A. Pimazzoni, C. Poggi, B. Pouradier-Duteil, B. Segalini, A. Shepherd, M. Spolaore, C. Taliercio, M. Ugoletti, P. Veltri, B. Zaniol, R. Pasqualotto, Spatially resolved diagnostics for optimization of large ion beam sources, Rev. Sci. Instrum. 93 (8) (2022) 081101, http://dx.doi.org/10.1063/5.0084797, arXiv:https://doi.org/10.1063/5.0084797.

[28] U. Fantz, S. Briefi, A. Heiler, C. Wimmer, D. Wünderlich, Negative hydrogen ion sources for fusion: From plasma generation to beam properties, Front. Phys. (2021) http://dx.doi.org/10.3389/fphy.2021.709651, Low-temperature Plasma Physics. URL https://www.frontiersin.org/articles/10.3389/fphy.2021.709651/full#h11.

[29] M. Bandyopadhyay, A. Tanga, H.D. Falter, P. Franzen, B. Heinemann, D. Holtum, W. Kraus, K. Lackner, P. McNeely, R. Riedl, E. Speth, R. Wilhelm, Analysis of plasma dynamics of a negative ion source based on probe measurements, J. Appl. Phys. 96 (8) (2004) 4107–4113, http://dx.doi.org/10.1063/1.1787619, arXiv:https://doi.org/10.1063/1.1787619.